



Article

Hydrogenated Amorphous Titania with Engineered Surface Oxygen Vacancy for Efficient Formaldehyde and Dye Removals under Visible-Light Irradiation

Guang Feng ^{1,2}, Mengyun Hu ^{1,2,3}, Botao Wu ³, Shencheng Shi ³, Shuai Yuan ^{1,2}, Yanan Li ³ and Heping Zeng ^{2,3,*}

- ¹ School of Optical-Electrical and Computer Engineering, University of Shanghai for Science and Technology, Shanghai 200093, China; 191380035@st.usst.edu.cn (G.F.); myhu@phy.ecnu.edu.cn (M.H.); syuan@usst.edu.cn (S.Y.)
- ² Chongqing Key Laboratory of Precision Optics, Chongqing Institute of East China Normal University, Chongqing 401120, China
- ³ State Key Laboratory of Precision Spectroscopy, East China Normal University, Shanghai 200062, China; btwu@phy.ecnu.edu.cn (B.W.); 51190920037@stu.ecnu.edu.cn (S.S.); 51200920008@stu.ecnu.edu.cn (Y.L.)
- * Correspondence: hpzeng@phy.ecnu.edu.cn

Abstract: Hydrogenated crystallized TiO_{2-x} with oxygen vacant (O_V) doping has attracted considerable attraction, owing to its impressive photoactivity. However, amorphous TiO_2 , as a common allotrope of titania, is ignored as a hydrogenated template. In this work, hydrogenated amorphous TiO_{2-x} (HAM- TiO_{2-x}) with engineered surface O_V and high surface area ($176.7 \text{ cm}^2 \text{ g}^{-1}$) was first prepared using a unique liquid plasma hydrogenation strategy. In HAM- TiO_{2-x} , we found that O_V was energetically retained in the subsurface region; in particular, the subsurface O_V -induced energy level preferred to remain under the conduction band (0.5 eV) to form a conduction band tail and deep trap states, resulting in a narrow bandgap (2.36 eV). With the benefits of abundant light absorption and efficient photocarrier transportation, HAM- TiO_{2-x} coated glass has demonstrated superior visible-light-driven self-cleaning performances. To investigate its formaldehyde photodegradation under harsh indoor conditions, HAM- TiO_{2-x} was used to decompose low-concentration formaldehyde (~0.6 ppm) with weak-visible light ($\lambda = 600 \text{ nm}$, power density = 0.136 mW/cm^2). Thus, HAM- TiO_{2-x} achieved high quantum efficiency of 3×10^{-6} molecules/photon and photoactivity of 92.6%. The adsorption capabilities of O_2 (−1.42 eV) and HCHO (−1.58 eV) in HAM- TiO_{2-x} are both largely promoted in the presence of subsurface O_V . The surface reaction pathway and formaldehyde decomposition mechanism over HAM- TiO_{2-x} were finally clarified. This work opened a promising way to fabricate hydrogenated amorphous photocatalysts, which could contribute to visible-light-driven photocatalytic environmental applications.



Citation: Feng, G.; Hu, M.; Wu, B.; Shi, S.; Yuan, S.; Li, Y.; Zeng, H. Hydrogenated Amorphous Titania with Engineered Surface Oxygen Vacancy for Efficient Formaldehyde and Dye Removals under Visible-Light Irradiation. *Nanomaterials* **2022**, *12*, 742. <https://doi.org/10.3390/nano12050742>

Academic Editor: Francesc Viñes Solana

Received: 5 January 2022

Accepted: 16 February 2022

Published: 22 February 2022

Publisher's Note: MDPI stays neutral with regard to jurisdictional claims in published maps and institutional affiliations.



Copyright: © 2022 by the authors. Licensee MDPI, Basel, Switzerland. This article is an open access article distributed under the terms and conditions of the Creative Commons Attribution (CC BY) license (<https://creativecommons.org/licenses/by/4.0/>).

Keywords: amorphous TiO_2 ; oxygen vacancy; bandgap; formaldehyde; visible light

1. Introduction

As a promising and environmentally-friendly photocatalyst, titanium dioxide (TiO_2) has gained widespread traction in the past few decades [1–5]. In order to pursue the best performance in solar energy conversion and utilization, one of the most effective approaches in tuning the band structure and maximizing solar energy capture is O_V defect engineering of TiO_2 [6–9]. Among considerable strategies in O_V defect engineering, the most representative and effective one is thermal hydrogenation of crystallized TiO_2 , which promotes the generation of O_V -doped disordered surface at crystalline TiO_2 , i.e., a disordered surface at the crystalline core [9–12]. This unique configuration not only provides additional O_V -induced states to absorb long-wavelength light, thereby enabling colorful TiO_{2-x} , but also encourages photoinduced charge separation to achieve superior visible-light photoactivity [13–15]. To obtain photocatalysts with superior efficiency, the polymorph

modifications of crystalline titanium dioxide also attracted much attention [16,17]. Alternatively, compared with crystalline TiO_2 , amorphous TiO_2 , which also exhibits an intrinsic narrow bandgap, thermodynamic metastability, and a large surface area, should be a great promising templet for surface hydrogenation [18–20]. Nevertheless, inherent drawbacks, including large quantities of bulk defects and inferior solar energy conversion eliminate this possibility. Theoretically, hydrogenated amorphous TiO_{2-x} (HAM- TiO_{2-x}) ought to have a narrower bandgap and more surface- O_V -induced active sites, which are the crucial factors for high-visible photoactivity. However, in practice, thermal hydrogenation using amorphous TiO_2 is ineluctable to require a long annealing process, which completely transforms the product into hydrogenated crystalline TiO_{2-x} and easily erases the surface O_V . Given the above challenges in the synthesis theory and technology, hydrogenation of pure amorphous phase TiO_2 has so far scarcely succeeded. Considering these aspects, the goal of this work is to prepare HAM- TiO_{2-x} with an O_V -doped disordered surface (disordered surface at the amorphous core) and, particularly, to reveal the fundamental mechanism of the correlation between O_V concentration and distribution, electrical structure, optical response, reactive oxygen species (ROS) generation, and its photoactivity, which can discover uncommon electrical and optical properties of HAM- TiO_{2-x} better than traditional hydrogenated crystalline TiO_{2-x} .

Formaldehyde, one of the most common indoor air pollutions, is highly poisonous and carcinogenic and is an immense threat to human health [21,22]. Photocatalytic formaldehyde purification is an efficient and safe method that can completely decompose formaldehyde into carbon dioxide and water [23–27]. Current studies on photocatalytic formaldehyde photodegradation are mainly focused on reaction mechanisms, such as peculiar formaldehyde physicochemical adsorption models and complex reaction pathways. In particular, they are focused on the synthesis of advanced photocatalysts with superior formaldehyde degradation performance under standard and ideal experimental conditions, including high power density of UV light source, high concentration formaldehyde, as well as high reaction temperature and pressure. However, in a practical indoor environment the situation is completely inverse: a practical indoor environment provides low-concentration formaldehyde (0.2–0.5 ppm), a weak-visible-light illumination (0.1–0.3 mW/cm²), and indoor temperature (25 °C). Photocatalysts with inferior visible-light response and photocarrier transferring cannot actively work under these conditions. More importantly, the ambient durability of photocatalysts should be stressed because of surface fouling/deactivation induced by dust and aerosol particles [28,29]. Herein, a photocatalyst must possess strong visible-light-driven photoactivity, a straightforward reaction pathway, and a self-cleaning surface with long-term stability. With the advantages of narrow bandgap, large specific surface area, and abundant surface O_V -induced active sites, HAM- TiO_{2-x} could be well suited for realistic formaldehyde purification.

In this work, we first reported the preparation of hydrogenated amorphous TiO_{2-x} nanoparticles and systematically expounded the effects of surface O_V on its optical bandgap, surface dynamics of photocarriers, and visible-light photoactivity. After functionalized surface hydrogenation by a liquid plasma strategy, the distribution and concentration of O_V in HAM- TiO_{2-x} can be designed well via manipulating the output power of liquid plasma discharge. According to density function theory simulations, one important finding was that the O_V concentration determined the existence of deep states in the bandgap, while the accurate energy level for these deep states was decided by the O_V distribution. Surface O_V -induced deep states were formed close to the valence band, whereas subsurface O_V -induced deep states were mainly generated under the conduction band. With the benefits of narrow bandgap and efficient charge carrier migration, HAM- TiO_{2-x} and its coating exhibited excellent visible-light dye degradation and stability. More importantly, low-concentration formaldehyde (0.6 ppm) was completely decomposed in an ambient environment using HAM- TiO_{2-x} . The durability test and apparent quantum efficiency of formaldehyde removal under visible light ($\lambda = 600$ nm, power density = 0.136 mW/cm²) were explored. In

addition, ROS generation, formaldehyde photodegradation pathway, chemical adsorption energy, and photocatalytic mechanism of HAm-TiO_{2-x} were investigated.

2. Experimental Section

2.1. Reagents and Materials

Titanium foam (99%, 100 mesh) and titanium rods (99%, 3-mm diameter) were acquired from Baoji Hong Xinyuan Metal Material Co., Ltd. (Baoji, China) P25 TiO₂ was purchased from Degussa (Evonik, Essen, Germany).

2.2. Preparation of HAm-TiO_{2-x}

One piece of anodic titanium foam (20 × 20 × 2 mm³) and two cathodic titanium rods (3-mm diameter) were placed in an electrical cell that filled with 300-mL nitric acid electrolyte (HNO₃), as shown in Figure 1A. Two cathodes were used to generate liquid plasma discharges and to avoid unbalanced flow, as well as to ensure sufficient hydrogenation effects at the double side of the Ti foam. The strong plasma on cathode surfaces was generated by supplying square wave impulse voltages between anodes and cathodes. A water-cooling machine was used to avoid electrolyte evaporation. The surface color of Ti foam varied from pale gray to charcoal gray after 1 h of liquid plasma treatment. Afterward, the gray titanium foam was put into a beaker filled with 20-mL deionized water and treated with an ultrasonic cleaner for 15 min to obtain a gray liquid, which was then dried with a microwave to obtain gray nanopowders, as shown in Figure 1B. All samples were obtained with the same treatment time (1 h), output voltage (700 V), and frequency (1 kHz) but with different output power. The radiation spectra of liquid plasma from 350 to 560 W were recorded in Figure S1. The resulting sample name was denoted by the output power of the liquid plasma, for example, AT-350 referred to HAm-TiO_{2-x} prepared by applying 350-W output power, AT-420 prepared with 420 W, AT-490 prepared with 490 W, and AT-560 prepared with 560 W.

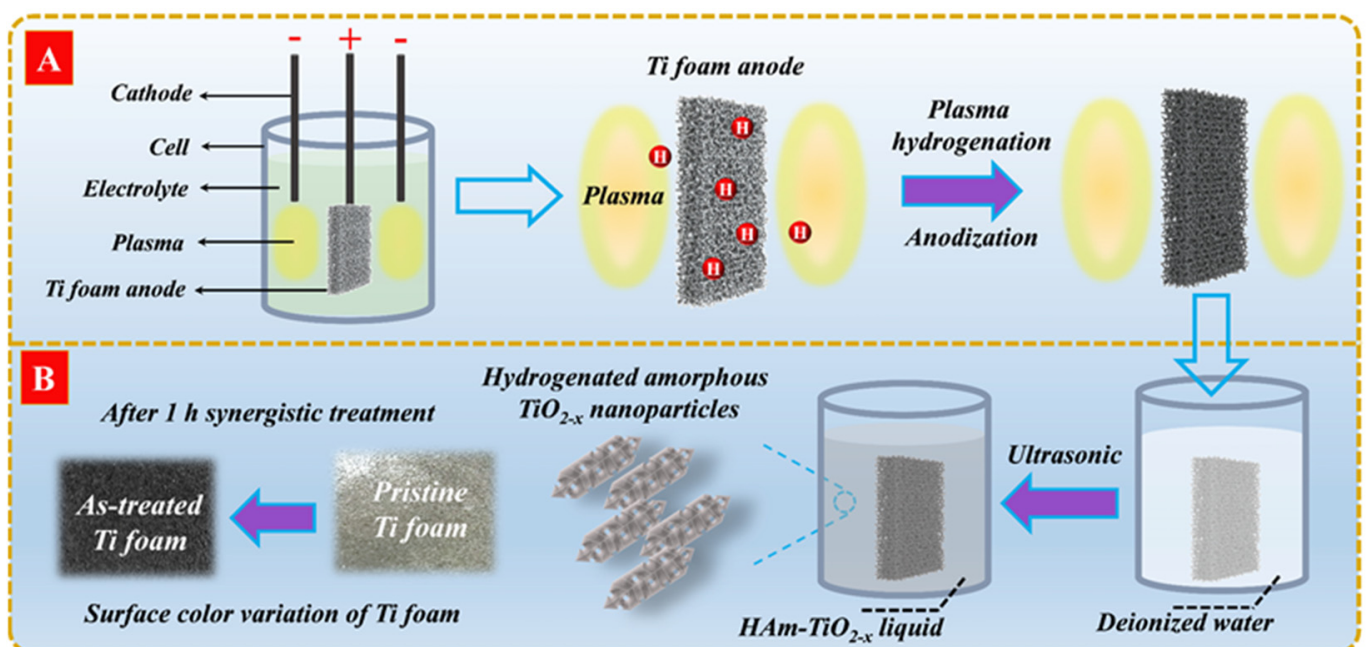


Figure 1. (A) Synthesis setup of producing HAm-TiO_{2-x}, and (B) the generation process of HAm-TiO_{2-x} nanoparticles.

2.3. Preparation of HAM-TiO_{2-x}-Coated Glass

HAM-TiO_{2-x} coated glass was prepared by impregnation method. First, to promote the surface hydrophilicity of the glass substrate, a corona discharger (Zhejiang Ruian Zhilin Corona Equipment Co., Ltd., Ruian, China) was used to make surface superhydrophilicity. Second, the treated glass substrate was put into a well-dispersed HAM-TiO_{2-x} liquid (AT-420, 0.1 mg/mL) for 1 min and was then taken out and dried with a microwave oven to deposit a thin HAM-TiO_{2-x} film on the glass.

2.4. Characterization

An X-ray powder diffraction instrument (XRD, Rigaku Smartlab, Rigaku, Tokyo, Japan) was used to analyze the crystallinity of HAM-TiO_{2-x}. The high-resolution morphology images were acquired by transmission electron microscopy (TEM, JEOL JEM-2100F, JEOL, Tokyo, Japan) with a 200-kV accelerating voltage. A scanning electron microscope (SEM, ZEISS MERLIN, ZEISS, Jena, Germany) was used to characterize the morphology and energy dispersive spectroscopy mapping using 5-kV acceleration voltage. Shimadzu UV-2700 (Shimadzu, Kyoto, Japan) was carried out to measure UV-Vis-diffused reflectance spectroscopy (DRS) at room temperature. A Micromeritics BET analyser (Micromeritics, Norcross, GA, USA) was used to characterize N₂ Brunauer, Emmett and Teller (BET) surface area and pore volume of HAM-TiO_{2-x}. X-ray photoelectron spectrum (XPS, Thermo Escalab 250Xi, Thermo Scientific, Waltham, MA, USA) was used to identify the valence state of surface elements. X-band electron paramagnetic resonance (EPR) was implemented to verify the lattice defects. The surface wetting ability of HAM-TiO_{2-x}-coated glass was measured using a contact angle meter (KINO SL200KB, KINO Scientific Instrument Inc., Boston, MA, USA). A fluorescence spectrophotometer (F-7100, Hitachi, Tokyo, Japan) was employed to record the photoluminescence spectra (PL) of HAM-TiO_{2-x} with 365-nm excitation wavelength. Electrochemical workstation (CHI660E, CH Instruments, Inc., Austin, TX, USA) was applied for measurement of photocurrent density. A Thermo Scientific DXR Raman microscope equipped with a 532-nm laser excitation was used to record Raman spectra at room temperature. X-band EPR spectra for active species trapping experiments were applied by using a Bruker EMX PLUS (Bruker, Billerica, MA, USA). In-situ diffused Fourier transform infrared spectroscopy (In-situ DRIFTS, PerkinElmer Spotlight 400, Waltham, MA, USA) was applied during formaldehyde photodegradation. The emitted spectra of liquid plasma discharge were recorded by a spectrometer (Ocean Optics Maya 2000 pro, Ocean Insight, Orlando, FL, USA).

The positron annihilation lifetime spectrum owns a ²²Na positron emission source and its activity is approximately 2×10^6 Bq. The positrons with a kinetic energy of 0–540 keV are produced when the source undergoes β^+ decay and, almost simultaneously, emits γ photons (1.28 MeV). Therefore, the appearance of this gamma photon can be regarded as the starting time for generating positrons; the appearance of 0.511 MeV annihilation gamma photons is the end of the positron annihilation event; this interval is the positron lifetime. The radioactive source is sandwiched between the sample to form a sandwich structure with a total of 2 million counts and, herein, the positron annihilation lifetime spectrum is already recorded. The time resolution of the system is approximately 190 ps, with a track width of 12.5 ps.

2.5. Photodegradation Experiments of HA-TiO_{2-x}

2.5.1. The Dyes Photodegradation of HAM-TiO_{2-x} Nanoparticles and Their Coatings

The photoactivity of HAM-TiO_{2-x} was assessed by photodegradation of rhodamine B (RhB) under visible light (420–800 nm). First, HAM-TiO_{2-x} nano-powders (50 mg) and RhB solution (20 mg/L, 50 mL) were put into a beaker with 60-min magnetic stirring for adsorption–desorption equilibrium. During photodegradation, 1-mL of solution was taken out from the beaker to test its absorbance at 554-nm wavelength via spectrophotometer. To evaluate the stability of HAM-TiO_{2-x}, AT-420 was preserved in water for 7 days for the subsequent use under the same experimental conditions. Furthermore, HAM-TiO_{2-x} coat-

ing was applied to decompose RhB and methyl blue (MB). For the RhB photodegradation experiment, a 2-mL RhB solution (20 mg/L) was dropped on the HAm-TiO_{2-x} coating (10 × 5 × 0.3 cm³), which was then dried in an oven for 10 min; afterward, the treated HAm-TiO_{2-x} coating was irradiated with visible light for 1 h. During the decomposition of MB, HAm-TiO_{2-x} coating (2 × 2 × 0.3 cm³) was immersed in a 10-mL MB solution (20 mg/L) to test its visible-light photoactivity.

The in-situ trap of spin-reactive species under visible-light illumination was recorded by the EPR signals of ·O₂⁻ and ·OH using 5,5-dimethyl-1-pyrroline-N-oxide (DMPO). In addition, in reactive species trapping experiments, the concentration of all sacrifice agents was 0.2 mM/mL, including ammonium oxalate (AO), Fe (II)-EDTA, potassium iodide (KI), p-benzoquinone (BQ), and isopropanol (IPA).

2.5.2. Formaldehyde (HCHO) Photodecomposition Test over HAm-TiO_{2-x}

Photocatalytic elimination of HCHO was performed in a sealed box (1 × 1 × 1 m³) at room temperature (25 °C, relative humidity = 52%) under visible-light irradiation. The xenon lamp was placed inside the box as the visible-light source, which was equipped with a bandpass filter glass centered at 600 nm (full width at half maximum (FWHM) = 15 nm). The HAm-TiO_{2-x} coating was deposited on a stainless-steel plate (3036 cm²) with a loading of 1 mg/cm²; afterward, this stainless-steel plate was placed below the xenon lamp. The power density of irradiated light on the stainless-steel plate was 0.136 mW/cm². A certain amount of 38% HCHO was injected into the sealed box; a 7-W fan was used to ensure proper HCHO diffusion. After dark adsorption-desorption equilibrium, the preliminary concentration of HCHO was approximately 0.6 ppm. During photodegradation, an HCHO tester (PPM-HTV, UK) was used to record the real-time HCHO concentrations. The HCHO photocatalytic formaldehyde mineralization efficiency (η) was measured by the equation: η (%) = (C₀ - C_t)/C₀ × 100%, where C₀ and C_t describe instant HCHO concentrations at 0 and t h, respectively. In addition, 365-nm UV light-mediated HCHO photodegradation was performed under the same conditions except for the light source.

Apparent quantum efficiency (AQY) of HCHO photodegradation was defined as Equations (1)–(3) [30]:

$$\text{AQY} = \frac{\text{number of degraded pollutant molecules}}{\text{number of photons entering the reactor}} \times 100\% \quad (1)$$

$$N_M = N_A \times n_{\text{HCHO}} = N_A \times ((C_0 - C_t) \times V) / (30 \times 1000) \quad (2)$$

$$\text{number of photons entering the reactor} = I \times S / (hc/\lambda) \times t \quad (3)$$

where N_M, N_A, n_{HCHO}, C₀, C_t, and V represent the number of degraded pollutant molecules, Avogadro's constant, moles of degraded HCHO, initial HCHO concentration, HCHO concentration of t h, and volume of the box, respectively. While I, S, h, c, λ, and t are illumination intensity, area, Planck's constant, the vacuum speed of light, the incident light wavelength, and illumination time, respectively.

2.6. Theoretical Calculation Methods

To complete all spin-polarization density functional theory (DFT) calculations, with the Perdew–Burke–Ernzerhof (PBE) formulation, the first-principles were employed within the generalized gradient approximation (GGA) [31–33]. The projected augmented wave (PAW) potentials were selected to illustrate the ionic cores and took valence electrons into account [34,35]. Through the Gaussian smearing method, partial occupancies of the Kohn–Sham orbitals were used with 0.05-eV width. When the energy change was lower than 10⁻⁴ eV, the electronic energy was regarded as self-consistent. When the energy change was lower than 0.05 eV Å⁻¹, a geometry optimization was identified as convergent; the vacuum spacing from the structural plane was 18 Å. The TiO₂ (101) amorphous structure was obtained by ab initio first-principles molecular dynamics (AIMD) simulation calculation with 20 ps using the 300 K. In addition, the TiO₂ (101) crystal structure had been optimized

using the AIMD simulations with the 1-fs step and 300 K; this crystal structure was then changed into amorphous TiO_2 (101). Finally, it was relaxed using DFT calculations in order to obtain the TiO_2 (101) stable amorphous structure.

3. Results and Discussion

3.1. Characterization of HAM- TiO_{2-x}

Figure 2A exhibits the XRD patterns for all HAM- TiO_{2-x} . Here, we provided two XRD cards of crystalline TiO_2 -involved anatase (PDF#21-1272) and rutile (PDF#21-1276). No apparent peaks indexed to crystalline phase are detected, but the weak and broad peaks at (101) facet of all samples compared with that of P25 TiO_2 indicates that a long-term disordered defect was generated. Figure S2 displays the surface atomic bond environment of all samples by Raman spectra. The observed broad and blue shift of E_g mode in our case could be ascribed to the surface oxygen vacancies in HAM- TiO_{2-x} [36]. Figure 2B shows the light response performance of all HAM- TiO_{2-x} using DRS spectra. All samples display enhanced visible light absorption; the bandgaps of AT-350, AT-420, AT-490, and AT-560 are estimated to be 2.74, 2.36, 2.57, and 2.91 eV, respectively. The plots of $(\alpha h\nu)^{1/2}$ versus $h\nu$ by using the Kubelka–Munk function were seen in Figure S3. Given the above results, some self-doped defects should exist in HAM- TiO_{2-x} . To verify the existence of the surface defect on HAM- TiO_{2-x} , EPR spectrum was implemented, as seen in Figure 2C. A sharp EPR signal of $g = 2.004$ is evidence that the AT-420 sample possessed oxygen vacancies [37]. In addition, Figure 2D illustrates the size and structure of the nanopore using nitrogen adsorption–desorption isotherms. The pore structure in HAM- TiO_{2-x} was irregular, which was proven by the as-obtained typical IV curves with hysteresis loops. It was indicated that micropores and/or mesoporous were formed, owing to the hysteresis with the P/P_0 range of 0.7–0.9; the pore size was nearly 3.4 nm, as displayed in the inset. The large BET ($176.7 \text{ cm}^2 \text{ g}^{-1}$) and pore volume ($0.33 \text{ cm}^3 \text{ g}^{-1}$) in HAM- TiO_{2-x} both contribute to the large capturing of polluted molecules.

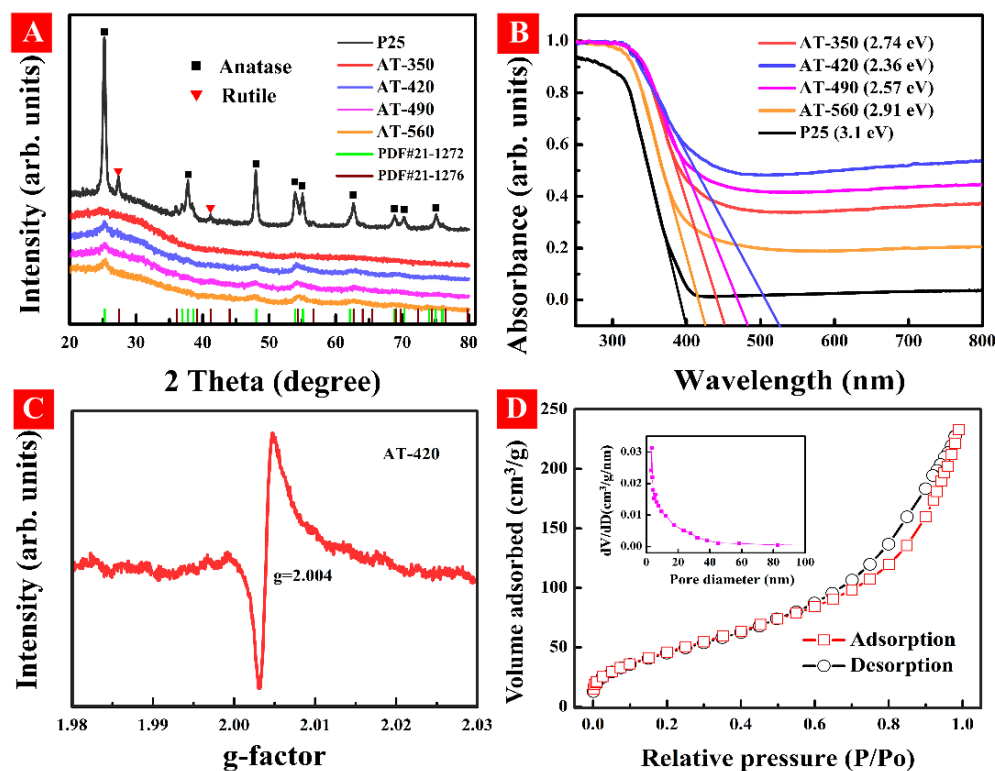


Figure 2. (A) The X-ray diffraction (XRD) patterns and (B) UV-vis diffuse-reflectance spectra for all as-prepared samples. (C) EPR spectrum and (D) nitrogen adsorption–desorption isotherms of AT-420 sample, inset is the pore diameter distribution calculated by the BJH method.

To investigate the morphology characterizations in HAM-TiO_{2-x}, TEM was conducted, as displayed in Figure 3. As shown in Figure 3A, HAM-TiO_{2-x} nanoparticles display irregular strip structure. As shown in Figure 3B, lots of textures marked with yellow rectangles exist in the nanoparticles, which seem similar to the leaf vein; these vein-like morphology features are deemed to be the irregular mesoporous structure. As shown in Figure 3C, a curve-like bulk defect marked with yellow oval was as roughly 20 nm long; furthermore, the disordered surface marked with yellow rectangle proves that surface amorphization with 1–2 nm thickness is prepared after liquid plasma treatment. No long-term range crystalline structure was observed, but some crystal lattices ($d = 0.353$ nm) of anatase (101) facet existed in HAM-TiO_{2-x}, which was in good accordance with the XRD results in Figure 2A. Figure 3D exhibits several nanopores marked with yellow circles with lengths of 2–3 nm, which is classified into mesopore and in good consistency with Barrett-Joyner-Halenda (BJH) result. Overall, HAM-TiO_{2-x} not only possesses the typical characteristics of amorphous materials, including long-term disorder lattice and large specific surface area, but also has broad visible-light harvest and disordered surface on the amorphous core.

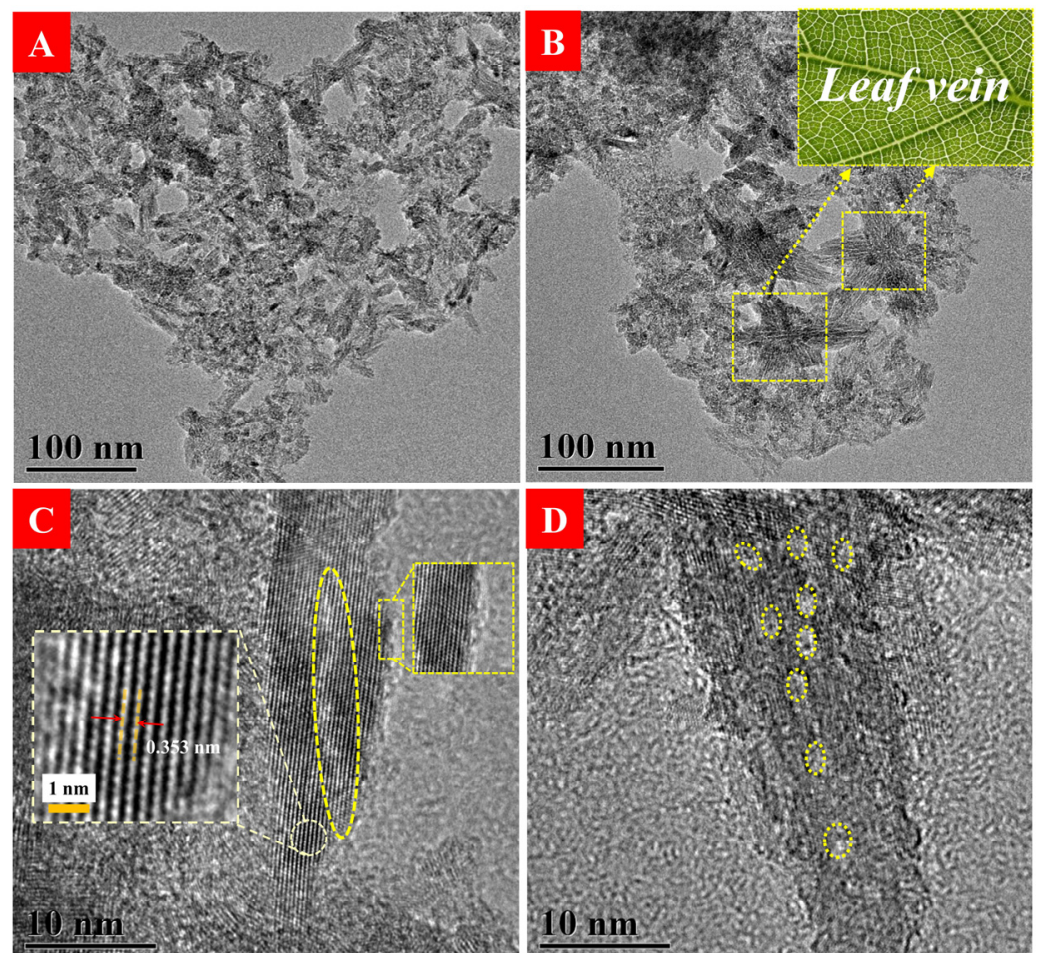


Figure 3. (A) Low magnification TEM images of HAM-TiO_{2-x}. (B) The leaf-vein-shaped nanoparticles in HAM-TiO_{2-x}, the inset was a photograph of the leaf vein. (C) The curve-like bulk defect marked with yellow oval and the disordered surface marked with yellow rectangle; the crystal plane spacing (d -spacing) was calculated to be 0.353 nm as shown in the left dotted box. (D) Some mesoporous structures marked with yellow circles in HAM-TiO_{2-x}.

3.2. Regulation of Surface O_V and Bandgap Engineering in HAM-TiO_{2-x}

Positron annihilation spectrometry (PAS) is a powerful tool that can be used to characterize the size, type, concentration, and distribution of surface defects in nanomaterials. As listed in Table 1, the relative intensities of three positron lifetime components denoted as τ_1 , τ_2 , and τ_3 are I_1 , I_2 , and I_3 , respectively. The largest component (τ_3) is generally regarded as the signal of large voids [38]. The second-largest lifetime component (τ_2) can be attributed to larger size defects, for instance, O_V clusters or surface defects [39]. The smallest component (τ_1) is responsible for free positrons annihilation with the lattice and at small O_V sites on the subsurface [40]. When the output power increased (AT-350 to AT-420), I_1 decreased, while I_2 increased, and, notably, I_3 of AT-420 was too small to detect. This observation indicates that the lattice O_V moved to the surface to form surface O_V , which was then accumulated on the catalyst surface and, thus, shielded the LV signal. With a further increase in output power (from AT-420 to AT-560), I_1 increased but I_2 decreased; both the intensities of I_3 for AT-420 and AT-490 were not detected, whereas I_3 of AT-560 emerged. It was, therefore, concluded that surface O_V moved back to the inner lattice to form subsurface O_V in sample AT-560. In conclusion, these results confirm that the output-power-regulated O_V not only distributed on the surface but also on the subsurface, rather than merely accumulating on the catalyst surface. More importantly, O_V in HAM-TiO_{2-x} existed preferentially at the subsurface if it underwent strong liquid plasma treatment. Compared with the surface O_V , subsurface and inner-bulk O_V are considered quite stable, as the outermost amorphous layer can prevent gradual oxidation by air and water [19,41]. The occurrence of the “roundtrip” path of O_V in HAM-TiO_{2-x}, as will be discussed further in what follows, could be a result of the synergistic effect of liquid plasma-induced hydrogenation and anodization.

Table 1. Positron lifetime and relative intensities of HAM-TiO_{2-x}, where the O_{VL} , O_{VS} , and LV are attributed to lattice O_V , surface O_V , and large voids, respectively.

Sample	τ_1 (ns)	O_{VL} - I_1 -%	τ_2 (ns)	O_{VS} - I_2 -%	τ_3 (ns)	LV- I_3 -%
AT-350	0.323	77.1	0.453	22.6	5.142	0.3
AT-420	0.224	10.8	0.363	89.2	/	/
AT-490	0.247	15.4	0.369	84.6	/	/
AT-560	0.329	87.8	0.526	11.8	3.797	0.4

To inspect the surface chemical states, XPS spectra were performed in HAM-TiO_{2-x}. As seen in full XPS spectra of Figure 4A, the lack of obvious differences between these samples demonstrated that the element components were identical. As shown in Figure 4B, P25 TiO₂ had two typical binding energies of Ti 2p_{3/2} (459.2 eV) and Ti 2p_{1/2} (465.2 eV) attributed to Ti⁴⁺ peaks [42,43]. In comparison, an apparent shift toward lower binding energies was observed for the sample AT-420, which suggested that Ti³⁺ existed on the disordered surface. We, thus, subtracted the Ti 2p spectra of P25 TiO₂ from that of sample AT-420, as seen in the bottom of Figure 4B; the resultant orange spectrum curve received two evident peaks (458.2 and 463.7 eV) ascribed to the Ti³⁺ (Ti 2p_{3/2} and Ti 2p_{1/2}) [44,45]. To calculate the ratio of Ti³⁺/Ti⁴⁺, the deconvoluted spectra of Ti 2p are provided in Figure 4C; the ratio was calculated by the areas of Ti³⁺ and Ti⁴⁺ at Ti 2p_{3/2} [46]. The highest Ti³⁺/Ti⁴⁺ ratio in AT-420 confirmed the highest concentration of Ti³⁺ in these samples, which is consistent with the PAS results; the detailed data regarding the Ti³⁺/Ti⁴⁺ ratio are displayed in Table 2. As shown in Figure 4D, three kinds of high-resolution O 1s peaks were observed, which were considered as the lattice oxygen (lattice O, 530.1 eV), surface oxygen defects (O deficiency, 531.9 eV), and hydroxyl group oxygen (hydroxyl O, 533.1 eV) [47,48]. As comparison, a much stronger peak intensity of O deficiency in AT-420 demonstrated a higher content of surface O_V . Furthermore, the clear shift toward lower binding energy for the lattice O peak observed in sample AT-420 was due to the high-density surface oxygen vacancies [49]. Therefore, as shown in Figure 4B–D, compared with P25 TiO₂, an

apparent blue shift (0.1 eV) in Ti 2p and O 1s spectra were observed, which confirmed the existence of surface defects of Ti^{3+} and O_V on the disordered surface. To clarify the effect of Ti^{3+} concentration on bandgap structure modification, the XPS valence band maximum (VBM) spectra of HAM-TiO_{2-x} were investigated, as shown in Figure S4. The estimated VBM value for all samples was recorded in Table 2. Herein, according to Table 2, the band structures for all samples are displayed in Figure 5. It is clear that sample AT-420 exhibited the highest position of the valence band, which could induce a strong redox reaction and higher photoactivity. Notably, the electric potential of h^+ was higher than all samples, indicating that it is possible to disable UV-light-induced photoactivity in HAM-TiO_{2-x}. Here, the output-power-controlled bandgap engineering in HAM-TiO_{2-x} was realized, which was obtained via the regulation of the distribution and the concentration of O_V .

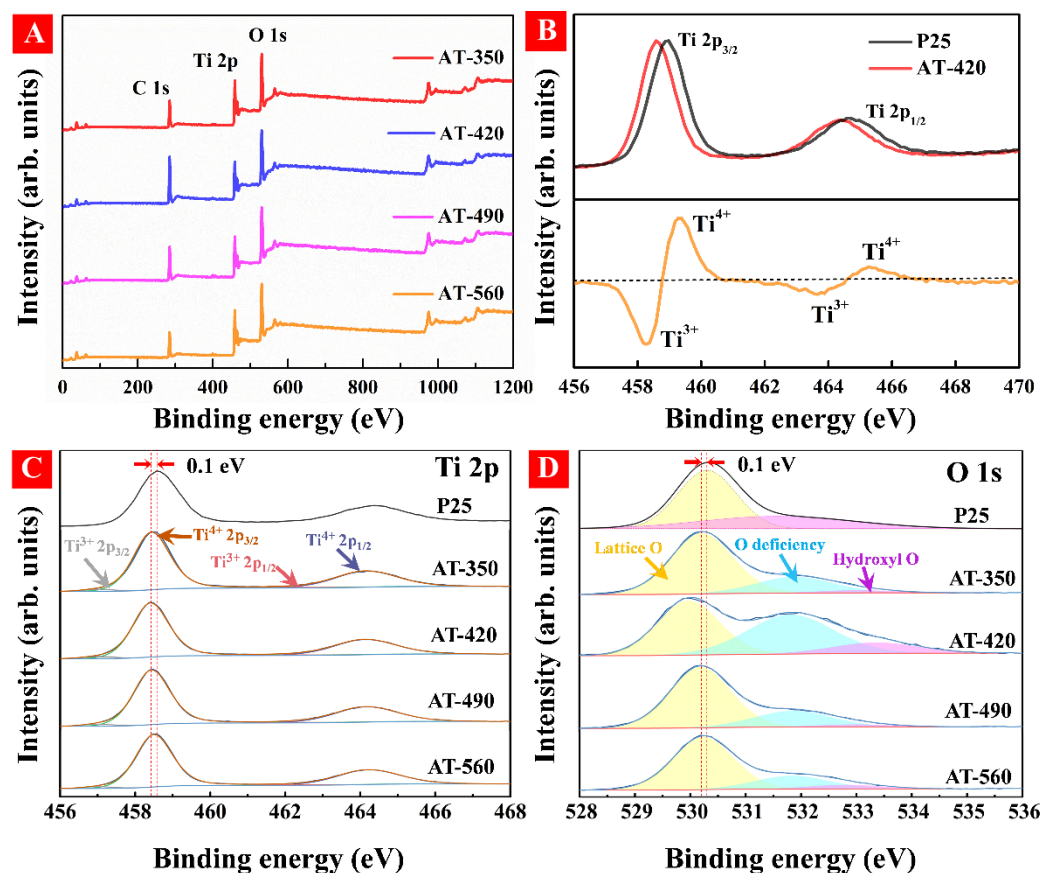


Figure 4. (A) Full XPS spectra for all samples, (B) Ti 2p spectra of AT-420 and P25 TiO₂. The deconvoluted Ti 2p (C) and O 1s (D) spectra for all samples.

Table 2. Bandgap, valence band maximum, and $\text{Ti}^{3+}/\text{Ti}^{4+}$ ratio of the HAM-TiO_{2-x} samples.

Sample	AT-350	AT-420	AT-490	AT-560
Output power (W)	350	420	490	560
Bandgap (eV)	2.74	2.36	2.57	2.91
VBM (eV)	2.48	2.16	2.33	2.58
Ratio of $\text{Ti}^{3+}/\text{Ti}^{4+}$	2.81%	3.01%	2.91%	2.69%

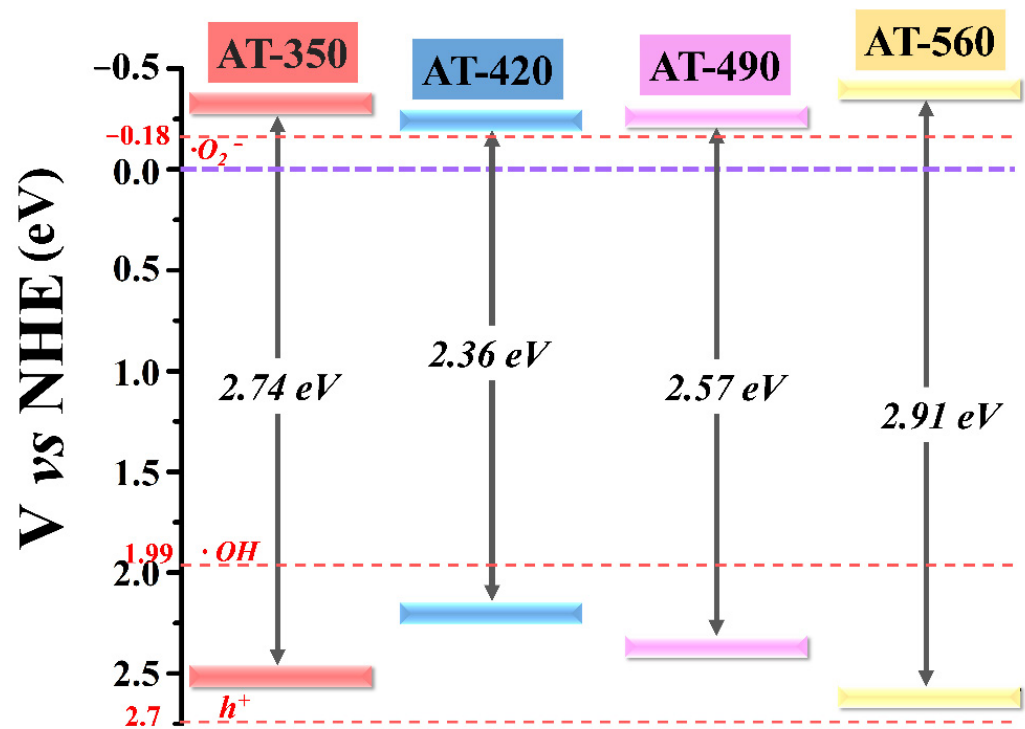


Figure 5. The bandgap structures of all samples.

3.3. Effect of Distribution and Concentration of O_V on Electrical Structure

The above PAS and XPS results indicated that the bandgap engineering of HAM-TiO_{2-x} could be directly achieved via the regulation of the distribution and concentration of O_V . However, an in-depth understanding of the effect of distribution and concentration of O_V on the regulation mechanism of the refined bandgap structure was still missing. Thus, DFT calculations regarding the effect of distribution and concentration of O_V on the electrical structures of HAM-TiO_{2-x} were carried out here. To balance the distribution and concentration of O_V , we used five kinds of atomic models, denoted as: Surface-1 O_V , Surface-4 O_V , Surface-2 O_V and Subsurface-2 O_V , Subsurface-1 O_V , and Subsurface-4 O_V , as depicted in Figure 6a–e, respectively. The naming system used here is such that the model of Surface-1 O_V represented the case in which one oxygen vacancy is located on the surface, and the model of Surface-2 O_V and Subsurface-2 O_V denoted two oxygen vacancies on the surface and two oxygen vacancies at the subsurface. The electronic band structures and density of states (DOS) of all models are displayed in Figure 6f–j. With the increase in the amount of surface O_V (Surface-1 O_V to Surface-4 O_V), deep trap states were generated above the valence band (~ 0.6 eV), and the flat deep states indicated large effective mass and restricted charge mobility, which led to photocarrier recombination. Owing to the introduction of deep states, some potential transitions may occur, including valence band to O_V -induced deep states (VB- O_{VS}), valence band to conduction band (VB-CB), and O_V -induced deep states to the conduction band (O_{VS} -CB), as depicted in Figure 6g. When the surface O_V moved to the inner domain to form subsurface O_V (Surface-4 O_V to Surface-2 O_V and Subsurface-2 O_V), deep trap states upshifted near the conduction band (~ 0.5 eV). In comparison with O_{VS} -CB transition in the Surface-4 O_V model, the transition observed in Surface-2 O_V and Subsurface-2 O_V was of much lower energy, which could induce a longer wavelength photoresponse, as shown in Figure 6h. When surface O_V moved entirely into the inner region (Subsurface-1 O_V), as depicted in Figure 6d, deep trap states disappeared, but several conduction band tails emerged, as shown in Figure 6i, which resulted in a much narrower bandgap. By further increasing subsurface O_V (Subsurface-4 O_V), as seen in Figure 6j, deep trap states close to the conduction band (~ 0.5 eV) reemerged. In summary, the O_V concentration determined the existence of deep trap states in the bandgap, and the O_V distribution determined their exact location. High concentration of surface O_V could

introduce the deep trap states, while O_V at the subsurface could upshift the deep trap states. On the basis of the PAS results, subsurface O_V was a substantial support in HAM-TiO_{2-x}, which suggests that the refined electrical structure of HAM-TiO_{2-x} could follow the model of Subsurface-4 O_V , generating deep trap states near the conduction band.

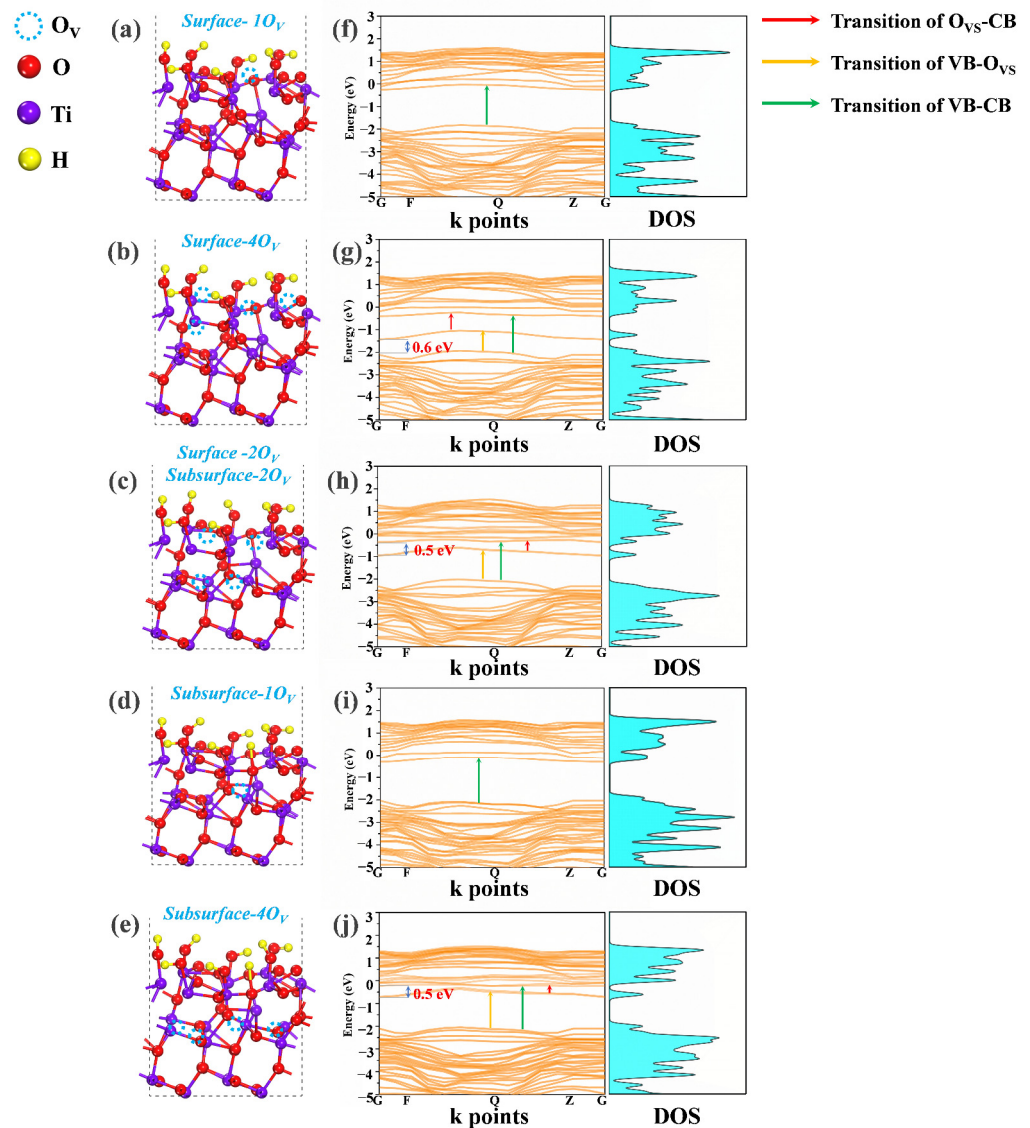


Figure 6. Five kinds of atomic models are shown in (a–e), respectively, and the corresponding band structure and DOS are shown in (f–j).

3.4. The Photo-Generated Carrier Activity of HAM-TiO_{2-x}

To explore the influence of subsurface O_V on the production and transferability of photogenerated charge carriers, the transient photocurrent density and PL spectra were explored using visible-light irradiation. As shown in Figure 7A, AT-420 displayed the highest photocurrent density among these samples, revealing the largest photoinduced carrier production and more efficient charge carrier separation. As displayed in Figure 7B, the PL spectra were measured to evaluate the photo-generated e–h pairs separation and transfer efficiency. It is clear that sample AT-420 exhibited the lowest intensity of all the samples, suggesting accelerated photoinduced carrier separation and transfer. Therefore, subsurface O_V in HAM-TiO_{2-x} contributed to the generation and transferring ability of photocarriers, which could greatly increase its visible-light photoactivity.

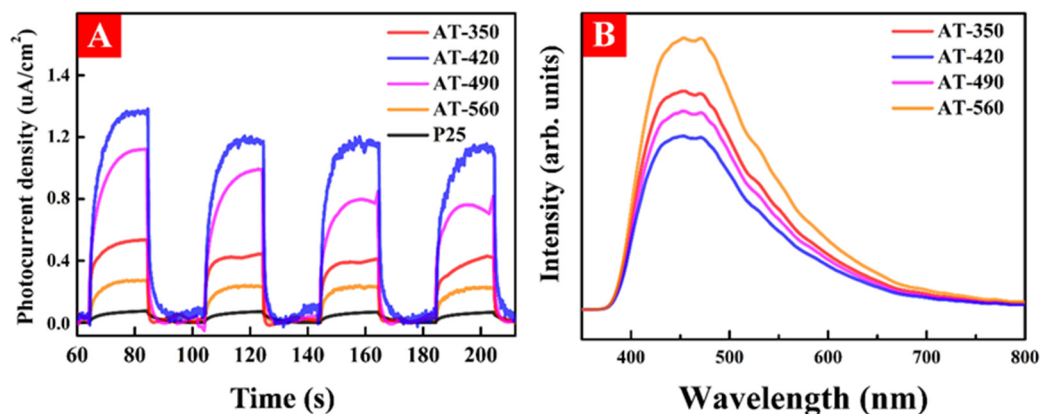


Figure 7. (A) The transient photocurrent density and (B) photoluminescence spectra for all samples.

3.5. The Visible-Light-Driven Photodegradation of HAM-TiO_{2-x} and Its Coatings

The visible-light photoactivity of HAM-TiO_{2-x} was evaluated by RhB photodegradation, shown in Figure 8A. During the dark adsorption, nearly 27.3% of RhB was removed by adsorption. AT-420 displayed the best performance among these samples, such that RhB photodegradation was accomplished within 20 min, owing to the fact that surface/subsurface O_V is generally considered unstable in air and water by the ambient oxidation, leading to faded photoactivity. Herein, to check the stability, AT-420 was put into deionized water for 7 days under ambient conditions for the aging test. Obviously, there was no clear difference between each round when using the aged AT-420 shown in Figure 8B, which proves that this surface/subsurface O_V in HAM-TiO_{2-x} was rather stable. In order to extend applications under various complicated environments, photocatalyst nanoparticles were usually deposited on diverse substrates, including glass, plastic film, and fiber. Herein, we urged the use of photocatalytic coating that has highly visible-light driven self-cleaning performance. We deposited HAM-TiO_{2-x} nanoparticles on glass (HAM-TiO_{2-x} @ glass, 10 × 5 × 0.3 cm³), which displayed an excellent photocatalytic self-cleaning performance when decomposing the dyes. As shown in Figure 8C, apart from the remaining high concentration “coffee ring” of RhB, most of the area became clean again. In addition, the visible-light photodegradation of methylene blue (MB) was also performed using the coated glass (2 × 2 × 0.3 cm³), as shown in Figure 8D, displaying a complete degradation of MB pollution. Therefore, according to the above polluted water photodegradation experiments, both HAM-TiO_{2-x} nanoparticles and its coatings enjoyed high visible photoactivity. Moreover, to detect ·OH and ·O₂⁻, EPR spin trapping experiments were employed over AT-420, with visible-light irradiation. As observed in Figure 8E, obvious signals of DMPO-OH and DMPO-O₂⁻ confirmed that ·OH and ·O₂⁻ were the dominant active oxygen species during photodegradation. Notably, the quantity of ·O₂⁻ was as much as seven times larger than that of ·OH listed in Table S1, which was generated by the surface O_V-absorbed electrons and which, simultaneously, verified the large quantities of surface/subsurface O_V. Actually, except for ·OH and ·O₂⁻, various reactive species, including ·OH_{ads} (·OH absorbed on the catalyst surface), photoinduced holes (h⁺), electrons, as well as H₂O₂, also participated during the photodegradation process. To explore the contribution from these reactive species, the trapping experiments were carried out over AT-420 using visible-light irradiation. Five kinds of scavengers, including AO, Fe(II)-EDTA, KI, BQ, and IPA were used to probe h⁺, H₂O₂, OH_{ads} and electron, ·O₂⁻, and ·OH in the bulk solution, respectively [50]. As shown in Figure 8F, the visible-light photodegradation rate without scavenger was 95.9%, while, in the presence of AO, Fe(II)-EDTA, KI, BQ, and IPA were 94.1%, 12.2%, 11.3%, 17.8, and 95.3%, respectively. It was, thus, confirmed that ·OH_{ads}, ·O₂⁻, and H₂O₂ were the dominated reactive species that contributed to high visible-light photoactivity, which is in good accordance with the EPR spin trapping results. However, h⁺ and ·OH in the bulk solution had almost no influence on photoactivity, which demonstrated that the generation of h⁺ was invalidated by preventing the transition of

electrons from the valence band to the conduction band or the O_V defect band, and was consistent with the band structures results, shown in Figure 5. The recycling experiment using AT-420 under visible light was carried out; the structural changes of the catalyst after usage are seen in Figure S5. Finally, the surface appearance of $HAm-TiO_{2-x}@glass$ was characterized by SEM, as seen in Figure 8G. According to 1- μm magnification SEM image, $HAm-TiO_{2-x}$ nanoparticles were uniformly coated on the glass surface, and the EDS mapping with 25- μm magnification also proved that Ti element was uniformly distributed on the glass surface. Increasing surface uniformity of $HAm-TiO_{2-x}$ nanoparticles can contribute to its photocatalytic activity. Due to the distribution of $HAm-TiO_{2-x}$ nanoparticles, the $HAm-TiO_{2-x}$ on the glass showed superhydrophilicity, which could increase the contact area between the catalyst and pollutant molecules, and which, thus, improved the photodegradation performance.

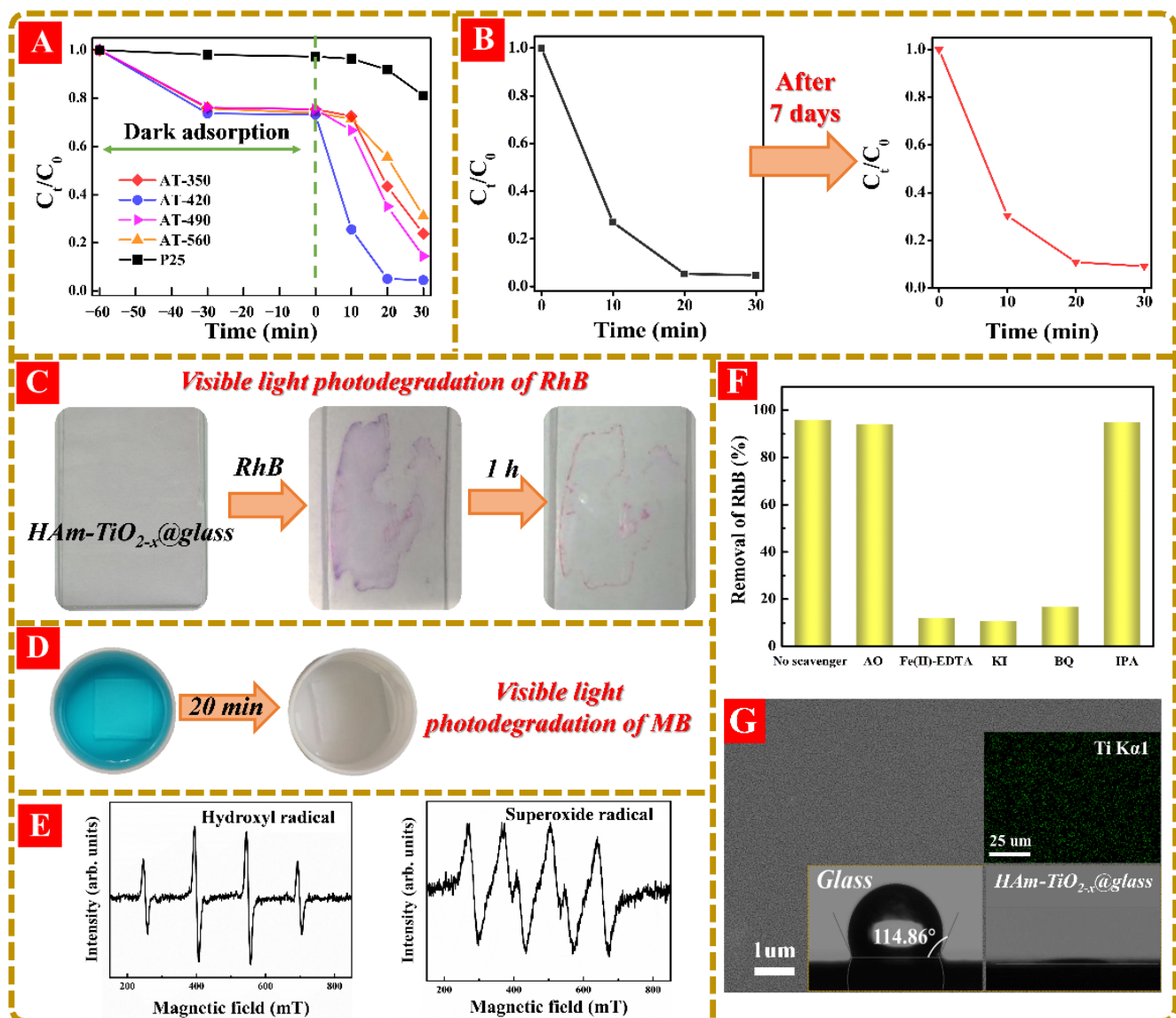


Figure 8. (A) The visible-light photodegradation of RhB for all samples and (B) the visible-light photodegradation stability test for AT-420. The visible-light photodegradations of (C) RhB and (D) MB using $HAm-TiO_{2-x}$ coated glass. (E) The EPR detection of $\cdot O_2^-$ and $\cdot OH$ over AT-420 under visible-light illumination. (F) The removal rates of AT-420 in the presence of different scavenging species. (G) Large-view SEM picture of $HAm-TiO_{2-x}@glass$ coated glass, the EDS mapping of Ti element and the hydrophilicity test in $HAm-TiO_{2-x}$ coated glass were shown in the inset.

3.6. The HCHO Photodegradation Activity under Ambient Environment

To investigate the formaldehyde (HCHO) photodegradation efficiency under ambient environment, a sealed box ($1 \times 1 \times 1 \text{ m}^3$) was used with simulated indoor conditions inside the box, including low HCHO concentration ($\sim 0.6 \text{ ppm}$), air atmosphere, indoor temperature ($\sim 25 \text{ }^\circ\text{C}$), relative humidity (RH = 45%), and low-power-density irradiation ($\lambda = 600 \text{ nm}$, 0.136 mW/cm^2). As shown in Figure 9A, HAM-TiO_{2-x} coating was put in the box for 1-h dark adsorption; the HCHO concentrations decreased slightly in the presence of all samples. During the visible light irradiation (0–18 h), gradual HCHO photodegradations were observed and followed a rank: AT-560 < AT-350 < AT-490 < AT-420, which also obeyed the rank of subsurface O_V concentration, as shown in PAS results. As an experimental comparison under the same condition, the HCHO concentration only decreased to 0.55 ppm using P25 TiO₂, owing to its poor visible light photodegradation. Notably, the final HCHO concentrations with AT-420 and AT-490 were both lower than 0.08 ppm, which is the international standard HCHO level for an indoor environment [51]. As shown in Figure 9B, the HCHO conversion efficiency increased rapidly in the initial stage of 0–4 h but reached saturation during 6–18 h; AT-420 exhibited the highest conversion efficiency of 92.62% (inset) among these samples. To verify the stability of HCHO photodegradation, a sustained release formaldehyde source was put in the box. As displayed in Figure 9C, the HCHO concentration linearly increased and, finally, reached 0.8 ppm in the absence of HAM-TiO_{2-x}. When AT-420 coating was put in the box, the HCHO concentration, as comparison, sharply increased during the 0–100 min, but trended to a steady value of 0.2 ppm with the increasing time, which suggested that a balance between the HCHO release and the photodegradation was achieved. More importantly, there was no upward tendency of HCHO concentration, demonstrating the strong and stubborn photoactivity of HAM-TiO_{2-x} that can erase the accumulation of HCHO and its by-products on catalyst surface. In addition, UV light of 365 nm assisted HCHO photodegradation, which was carried out using AT-420 coating, as shown in Figure 9D, which unexpectedly displayed poor photoactivity. Furthermore, the AQYs of HCHO photodegradation with different wavelengths of light were measured using AT-420 coating, as shown in Figure 9E. With the 600-nm light source, the AQY in the beginning of 0–2 h was nearly $3 \times 10^{-4}\%$ but decreased gradually during 3–18 h and reached $0.6 \times 10^{-4}\%$ eventually. While, with the 365-nm light source, the AQY exhibited a similar change tendency but was much lower than that of the 600-nm light source. Finally, relative humidity, as an important factor that affects HCHO photodegradation, should be explored. As displayed in Figure 9F, when RH during the visible-light photodegradation over AT-420 was 35%, the HCHO elimination efficiency was 80.7%. When increasing RH from 35% to 61%, the elimination efficiency was also enhanced from 80.7% to 98.3%, which could be ascribed to the adsorbed H₂O on HAM-TiO_{2-x} that contributed to the generation of $\cdot\text{OH}$ radical. When RH arrived at 73%, the HCHO decomposition efficiency, however, decreased to 88.7%, which should be a result of the competitive adsorption between H₂O and HCHO. Given the above results, HAM-TiO_{2-x} showed high and stable performance in HCHO photocatalytic elimination under the simulated indoor environment.

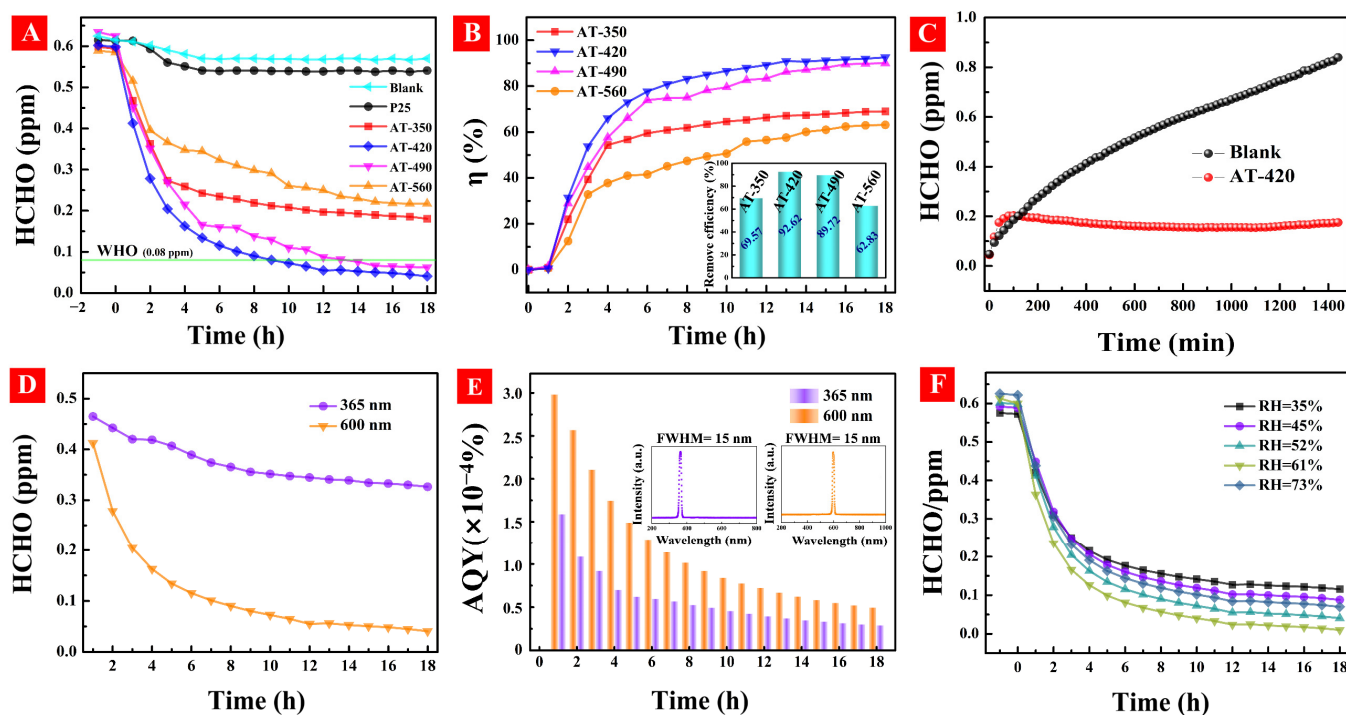


Figure 9. (A) Visible-light formaldehyde photodegradation and (B) the conversion efficiency with different samples, and the inset was the remove efficiency for all samples. (C) Durable test of AT-420 under simulated indoor conditions. (D) The HCHO photodegradations under 365-nm and 600-nm light sources using AT-420 sample. (E) The AQY of formaldehyde photodegradation with different wavelength light using AT-420 coating, and the inset were the spectra of UV (365 nm, FWHM = 15 nm) and visible (600 nm, FWHM = 15 nm) light. (F) The effect of relative humidity for AT-420 coating using 600-nm light source.

3.7. Investigations on the Surface Reaction Pathway and HCHO Adsorption Mechanism with the Subsurface O_V

In-situ DRIFTS analysis was employed to dynamically investigate the reaction pathways of HCHO photodegradation on HAM-TiO_{2-x} surface. As shown in Figure 10, the peaks at 1157 and 1200 cm⁻¹ were identified as HCHO [52,53]; the peaks at 1040, 1260, 1400, and 1633 cm⁻¹ were ascribed to carbonate species [54–57]; the peak at 1225 cm⁻¹ was considered as a formate species [58], while the peak at 3390 cm⁻¹ was considered as surface Ti-OH [23]. Observably, with the increasing irradiation time, the concentrations of all reactants, including formaldehyde, carbonate species, formate species, and surface hydroxyl groups were increased, suggesting that formaldehyde was absorbed on the HAM-TiO_{2-x} surface and oxidized by hydroxyl radicals into formate species and carbonate species. The main intermediates were carbonate species, which suggested the fast oxidation of HCHO and formate species. Thus, we inferred two potential photo-decompose paths of HCHO → HCOOH → H₂CO₃ → CO₂, and HCHO → HCOOH → CO₂. Unexpectedly, photocatalyst inactivation by this accumulated carbonate species and formate species did not occur, which was proven by the enhancement of surface hydroxyl groups with time. In light of these results and discussion, it was, thus, concluded that HAM-TiO_{2-x} possessed a straightforward reaction pathway and relevant strong photoactivity in HCHO photodegradation.

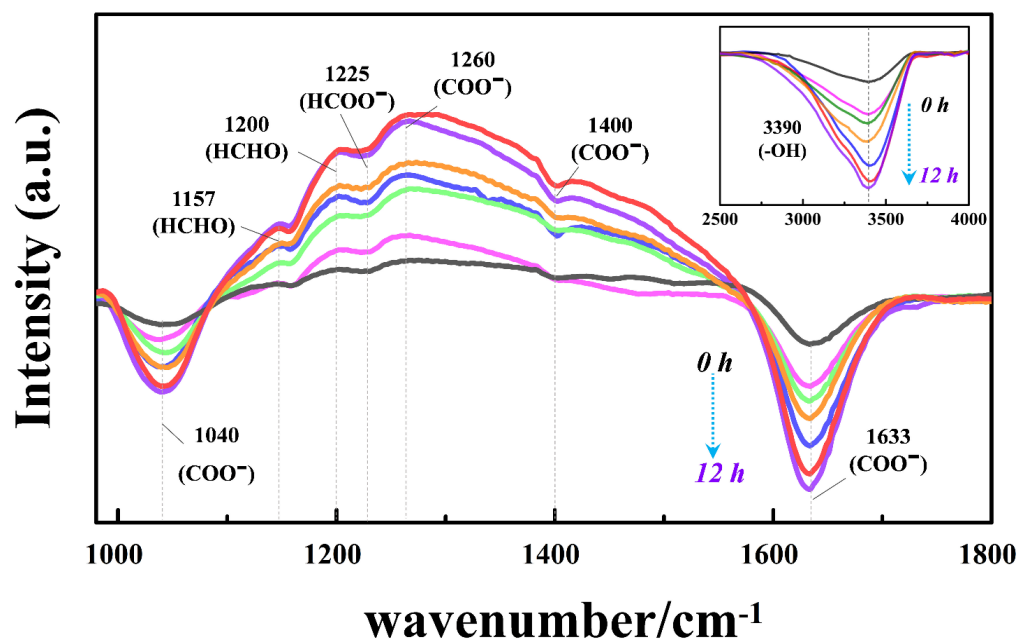


Figure 10. In-situ DRIFTS of AT-420 during the visible-light photodegradation of HCHO.

Generally, the photodegradation of HCHO is assumed to be determined by the synergistic effect of light absorption, photocarriers migration, reactants adsorption, and reaction pathway. Based on the aforementioned characterization results and discussion, HAM-TiO_{2-x} exhibited high performances in visible-light absorption, e-h pairs migration, and straightforward reaction pathways. Herein, reactants adsorption and, especially, the effect of surface hydroxyl group and O_V on chemisorb capability of HCHO and O₂, should be revealed. Here, we constructed two kinds of DFT-simulated adsorption models, including HAM-TiO_{2-x}-OH (the effect of surface hydroxyl group) and HAM-TiO_{2-x}-O_V (the effect of subsurface O_V) to investigate HCHO adsorption (Figure 11A) and O₂ adsorption (Figure 11B). Based on the DFT models, the adsorption energies of O₂ and HCHO on the surfaces of anatase TiO₂, HAM-TiO_{2-x}-OH, and HAM-TiO_{2-x}-O_V are exhibited in Figure 11C. Anatase TiO₂ showed the adsorption energies of -0.43 eV (O₂) and -0.81 eV (HCHO). When using HAM-TiO_{2-x}-OH, a lower adsorption energy of O₂ (-0.75 eV) and HCHO (-0.98 eV) were obtained. As for HAM-TiO_{2-x}-O_V, the corresponding adsorption energies were sharply decreased to -1.42 and -1.58 eV. Therefore, adsorption capabilities of O₂ and HCHO in HAM-TiO_{2-x} were both largely promoted in the presence of subsurface O_V, which could significantly promote the capturing of HCHO on the HAM-TiO_{2-x} photocatalyst and improve the HCHO photodegradation efficiency.

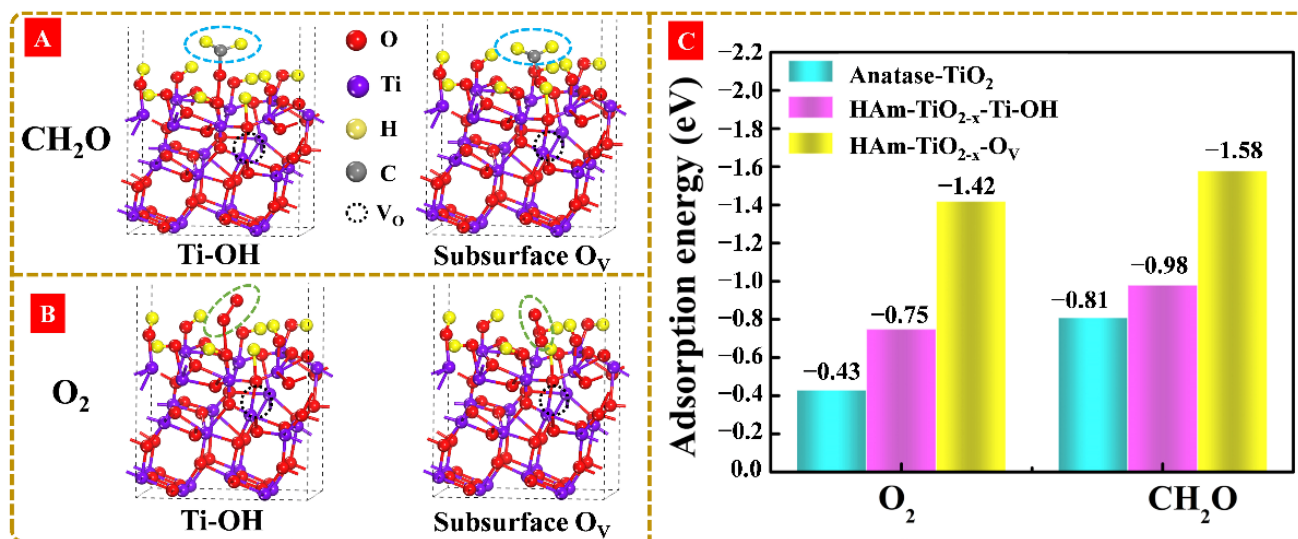


Figure 11. The adsorption models of (A) formaldehyde and (B) oxygen in the presence of surface hydroxyl groups and subsurface O_V, respectively. (C) The adsorption energies of O₂ and HCHO over anatase TiO₂, HAM-TiO_{2-x}-OH, and HAM-TiO_{2-x}-O_V.

3.8. The Mechanism of HCHO Photocatalysis and O_V Generation over HAM-TiO_{2-x}

Based on the above results and discussions, the photocatalysis mechanism of HCHO purification with HAM-TiO_{2-x} was illustrated in Figure 12. The refined electrical structure of HAM-TiO_{2-x} followed the band structures of the Subsurface-4O_V model, as mentioned in Figure 6e, which generated deep trap states close to the conduction band. When solar light irradiation—which has large effective mass—owing to the O_V-induced midgap trap states, restricts charge mobility, electrons from valence states are hardly transferred from valence band to O_V-induced deep states or conduction band, leading to bad photoactivity in the UV region. Visible-light capture in HAM-TiO_{2-x} is mainly originated from O_VS-CB transition, as mentioned in Figure 6. To some extent, HAM-TiO_{2-x}, with its self-doped O_V defects was, thus, customized for long-wavelength response photocatalysis. On the other hand, with the benefits of abundant surface O_V, photoinduced electrons had high separation efficiency and long lifetime, resulting in directional migration from the inner lattice to the top surface. Localized surface O_V accumulated a considerable number of electrons to react with O₂ and H₂O to form ·O₂⁻ and ·OH, which can rapidly decompose the adsorbed HCHO into CO₂, H₂O, and intermediates such as HCOOH and H₂CO₃. Moreover, contributed by subsurface O_V and surface hydroxyl radical (·OH), chemisorption energy of HAM-TiO_{2-x} was much lower than that of crystalline anatase TiO₂, resulting in the boosted adsorption capability of HCHO.

Finally, the formation mechanism of HAM-TiO_{2-x} nanoparticles should be clarified. In fact, apart from the generation of hydrogen atoms, liquid plasma discharge also produces many kinds of oxidative species including superoxide anion radicals, electrons, hydroxyl radical, hydrogen peroxide, and ultraviolet radiation, which enables strong oxygenation in electrolyte [59,60]. Herein, liquid plasma discharge involved two contrasting effects: liquid plasma hydrogenation and oxidation. Whether hydrogenation or oxidation dominates the whole reaction depends on the output power. Typically, hydrogenation plays a major role at a lower output power. With a proper increase of output power, hydrogenation is simultaneously enhanced and governs the reaction, but, when output power further increases and reaches a threshold, oxidation beyond hydrogenation dominates the whole reaction. In our case, compared with AT-350, a stronger hydrogenation effect was achieved with AT-420 (Figure S1), which resulted in a much higher O_V concentration. By further increasing output power (AT-420 to AT-560), surface O_V concentration declined, which could be due to the leading role of liquid plasma oxidation over the process. As a result, this alternate effect of hydrogenation and oxidation could also account for the “round-trip”

occurrence of O_V in $HAm-TiO_{2-x}$, as well as the rank of subsurface O_V concentration, listed as $AT-560 < AT-350 < AT-490 < AT-420$ (as seen in PAS and XPS data).

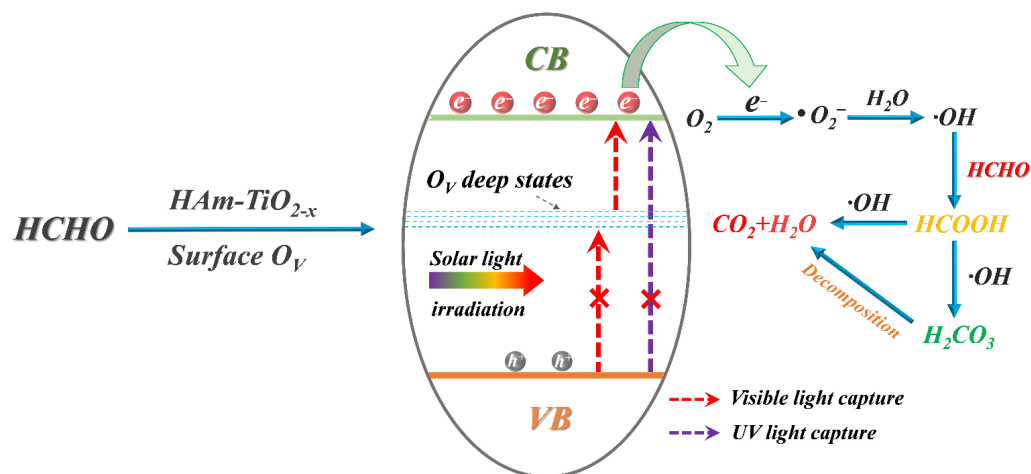


Figure 12. The proposed mechanism for photocatalytic elimination of HCHO with $HAm-TiO_{2-x}$.

4. Conclusions

In this work, hydrogenated amorphous TiO_{2-x} with high surface area ($176.7 \text{ cm}^2 \text{ g}^{-1}$) was successfully prepared using a liquid plasma-induced hydrogenation strategy. The effect of surface O_V engineering on the physico-chemical properties of amorphous TiO_2 photocatalyst and, in particular, the manipulation of O_V concentration and distribution on its electrical structure, was revealed. The optical and electrical properties of $HAm-TiO_{2-x}$ were affected by the surface O_V engineering, which could be directly regulated by controlling the output power of liquid plasma. Subsurface O_V , rather than surface O_V , induced a disordered surface, which accounted for the narrow bandgap (2.36 eV) by introducing deep trap states under a conduction band (0.5 eV). With the advantages of strong visible-light capture and efficient photocarriers transferring, $HAm-TiO_{2-x}$ and its coatings exhibited strong visible-light photodegradation of polluted water. Furthermore, $HAm-TiO_{2-x}$ was employed to decompose low-concentration formaldehyde under severe indoor environments. Investigations on the surface reaction pathway and formaldehyde adsorption mechanism with the subsurface O_V were also carried out. We found that subsurface O_V in $HAm-TiO_{2-x}$ could significantly enhance the adsorption energy of HCHO (-1.58 eV) and O_2 (-1.42 eV), compared with anatase TiO_2 . Based on large amounts of $\cdot OH$ radicals and strong chemisorption capability, $HAm-TiO_{2-x}$ showed high quantum efficiency of 3×10^{-6} molecules/photon and photoactivity of 92.6% under visible light ($\lambda = 600 \text{ nm}$). Sustaining growth of surface $\cdot OH$ radicals guaranteed long-term photocatalytic stability and disabled the surface deactivation of $HAm-TiO_{2-x}$. Owing to its superior photoactivity, extremely low cost, and simple preparation technology, hydrogenated amorphous TiO_{2-x} could be suitable for large production to apply in some practical photocatalytic environment purifications in the future.

Supplementary Materials: The following supporting information can be downloaded at: <https://www.mdpi.com/article/10.3390/nano12050742/s1>, Figure S1: The emission spectrum of liquid plasma with different output power, (A–D) are obtained by applying the output power of 350, 420, 490, and 560 W, respectively, Figure S2: Raman spectra of all $HAm-TiO_{2-x}$ samples, Figure S3: (A–D) were the Kubelka Munk graphs of AT-350 (2.64 eV), AT-420 (2.24 eV), AT-490 (2.51 eV), and AT-560 (2.89 eV), respectively, Figure S4: X-ray photoelectron spectroscopy valence band spectra of all samples, Figure S5: (A) The recycling experimental of RhB using AT-420 under visible light. (B,C) were EPR and XRD data for AT-420 and catalyst after recycling reaction, respectively. (D) High resolution TEM image of AT-420 after recycling reaction, and the disordered surface was marked with yellow dashed line, Table S1: The amount of $\cdot O_2^-$ and $\cdot OH$ by employing of 5,5-dimethyl-1-pyrroline-*N*-oxide (DMPO) to in-situ trap the spin-reactive species.

Author Contributions: G.F.: experimental measurements, material fabrication, manuscript preparation. B.W.: theoretical simulation, and manuscript reviewing. M.H., S.Y., Y.L. and S.S.: experiments and project discussions. H.Z.: photocatalyst design and experiments, project supervision, manuscript writing and reviewing. All authors have read and agreed to the published version of the manuscript.

Funding: This work was granted by National Key Research and Development Program of China (2018YFB0504400), National Natural Science Fund of China (11621404, 11727812, and 62035005), and Shanghai Science and Technology Commission (2019SHZDZX01-ZX06).

Institutional Review Board Statement: Not applicable.

Informed Consent Statement: Not applicable.

Data Availability Statement: The data presented in this study are available on request from the corresponding author. The data are not publicly available due to the reason that the data also forms part of an ongoing study.

Acknowledgments: This work was granted by National Key Research and Development Program of China (2018YFB0504400), National Natural Science Fund of China (11621404, 11727812, and 62035005), and Shanghai Science and Technology Commission (2019SHZDZX01-ZX06).

Conflicts of Interest: The authors declare no conflict of interest.

References

1. Fujishima, A.; Rao, T.N.; Tryk, D.A. Titanium dioxide photocatalysis. *J. Photoch. Photobiol. C* **2000**, *1*, 1–21. [[CrossRef](#)]
2. Rao, Z.; Lu, G.; Mahmood, A.; Shi, G.; Xie, X.; Sun, J. Deactivation and activation mechanism of TiO₂ and rGO/Er³⁺-TiO₂ during flowing gaseous VOCs photodegradation. *Appl. Catal. B Environ.* **2021**, *284*, 119813. [[CrossRef](#)]
3. Dagher, R.; Drogui, P.; Robert, D. Modified TiO₂ for environmental photocatalytic applications: A review. *Ind. Eng. Chem. Res.* **2013**, *52*, 3581–3599. [[CrossRef](#)]
4. Luciani, G.; Imparato, C.; Vitiello, G. Photosensitive hybrid nanostructured materials: The big challenges for sunlight capture. *Catalysts* **2020**, *10*, 103. [[CrossRef](#)]
5. Janczarek, M.; Endo-Kimura, M.; Raja-Mogan, T.; Kowalska, E. The role of oxygen vacancy and other defects for activity enhancement. In *Green Photocatalytic Semiconductors: Recent Advances and Applications*; Garg, S., Chandra, A., Eds.; Springer International Publishing: Cham, Switzerland, 2022; pp. 337–355.
6. Hao, L.; Huang, H.; Zhang, Y.; Ma, T. Oxygen vacant semiconductor photocatalysts. *Adv. Funct. Mater.* **2021**, *31*, 2100919. [[CrossRef](#)]
7. Zhang, Y.; Xu, Z.; Li, G.; Huang, X.; Hao, W.; Bi, Y. Direct observation of oxygen vacancy self-healing on TiO₂ photocatalysts for solar water splitting. *Angew. Chem. Int. Edit.* **2019**, *58*, 14229–14233. [[CrossRef](#)]
8. Li, J.; Zhang, M.; Guan, Z.; Li, Q.; He, C.; Yang, J. Synergistic effect of surface and bulk single-electron-trapped oxygen vacancy of TiO₂ in the photocatalytic reduction of CO₂. *Appl. Catal. B Environ.* **2017**, *206*, 300–307. [[CrossRef](#)]
9. Lin, L.; Ma, Y.; Wu, J.; Pang, F.; Ge, J.; Sui, S.; Yao, Y.; Qi, R.; Cheng, Y.; Duan, C.; et al. Origin of photocatalytic activity in Ti⁴⁺/Ti³⁺ core-shell titanium oxide nanocrystals. *J. Phys. Chem. C* **2019**, *123*, 20949–20959. [[CrossRef](#)]
10. Mao, J.; An, X.; Gu, Z.; Zhou, J.; Liu, H.; Qu, J. Visualizing the interfacial charge transfer between photoactive microcystis aeruginosa and hydrogenated TiO₂. *Environ. Sci. Technol.* **2020**, *54*, 10323–10332. [[CrossRef](#)]
11. Li, J.; Weng, B.; Cai, S.; Chen, J.; Jia, H.; Xu, Y. Efficient promotion of charge transfer and separation in hydrogenated TiO₂/WO₃ with rich surface-oxygen-vacancies for photodecomposition of gaseous toluene. *J. Hazard. Mater.* **2018**, *342*, 661–669. [[CrossRef](#)]
12. Yan, Y.; Cheng, X.; Zhang, W.; Chen, G.; Li, H.; Konkin, A.; Sun, Z.; Sun, S.; Wang, D.; Schaaf, P. Plasma hydrogenated TiO₂/Nickel foam as an efficient bifunctional electrocatalyst for overall water splitting. *ACS Sustain. Chem. Eng.* **2019**, *7*, 885–894. [[CrossRef](#)]
13. Zhang, K.; Park, J.H. Surface localization of defects in black TiO₂: Enhancing photoactivity or reactivity. *J. Phys. Chem. Lett.* **2017**, *8*, 199–207. [[CrossRef](#)]
14. Chen, X.; Liu, L.; Huang, F. Black titanium dioxide (TiO₂) nanomaterials. *Chem. Soc. Rev.* **2015**, *44*, 1861–1885. [[CrossRef](#)]
15. Wang, G.; Wang, H.; Ling, Y.; Tang, Y.; Yang, X.; Fitzmorris, R.C.; Wang, C.; Zhang, J.Z.; Li, Y. Hydrogen-treated TiO₂ nanowire arrays for photoelectrochemical water splitting. *Nano Lett.* **2011**, *11*, 3026–3033. [[CrossRef](#)] [[PubMed](#)]
16. Danyliuk, N.; Tatarchuk, T.; Kannan, K.; Shyichuk, A. Optimization of TiO₂-P25 photocatalyst dose and H₂O₂ concentration for advanced photo-oxidation using smartphone-based colorimetry. *Water Sci. Technol.* **2021**, *84*, 469–483. [[CrossRef](#)] [[PubMed](#)]
17. Tatarchuk, T.; Danyliuk, N.; Shyichuk, A.; Macyk, W.; Naushad, M. Photocatalytic degradation of dyes using rutile TiO₂ synthesized by reverse micelle and low temperature methods: Real-time monitoring of the degradation kinetics. *J. Mol. Liq.* **2021**, *342*, 117407. [[CrossRef](#)]
18. Kang, J.; Zhang, Y.; Chai, Z.; Qiu, X.; Cao, X.; Zhang, P.; Teobaldi, G.; Liu, L.; Guo, L. Amorphous domains in black titanium dioxide. *Adv. Mater.* **2021**, *33*, 2100407. [[CrossRef](#)]

19. Wang, B.; Biesold, G.M.; Zhang, M.; Lin, Z. Amorphous inorganic semiconductors for the development of solar cell, photoelectrocatalytic and photocatalytic applications. *Chem. Soc. Rev.* **2021**, *50*, 6914–6949. [[CrossRef](#)]
20. Sun, S.; Song, P.; Cui, J.; Liang, S. Amorphous TiO₂ nanostructures: Synthesis, fundamental properties and photocatalytic applications. *Catal. Sci. Technol.* **2019**, *9*, 4198–4215. [[CrossRef](#)]
21. Cheng, L.; Li, B.; Cheng, Q.; Baldwin, A.N.; Shang, Y. Investigations of indoor air quality of large department store buildings in China based on field measurements. *Build. Environ.* **2017**, *118*, 128–143. [[CrossRef](#)]
22. Chang, T.; Wang, J.; Lu, J.; Shen, Z.; Huang, Y.; Sun, J.; Xu, H.; Wang, X.; Ren, D.; Cao, J. Evaluation of indoor air pollution during decorating process and inhalation health risks in Xi'an, China: A case study. *Aerosol Air Qual. Res.* **2019**, *19*, 854–864. [[CrossRef](#)]
23. He, M.; Ji, J.; Liu, B.; Huang, H. Reduced TiO₂ with tunable oxygen vacancies for catalytic oxidation of formaldehyde at room temperature. *Appl. Surf. Sci.* **2019**, *473*, 934–942. [[CrossRef](#)]
24. Zhu, M.; Muhammad, Y.; Hu, P.; Wang, B.; Wu, Y.; Sun, X.; Tong, Z.; Zhao, Z. Enhanced interfacial contact of dopamine bridged melamine-graphene/TiO₂ nano-capsules for efficient photocatalytic degradation of gaseous formaldehyde. *Appl. Catal. B Environ.* **2018**, *232*, 182–193. [[CrossRef](#)]
25. Huang, Q.; Hu, Y.; Pei, Y.; Zhang, J.; Fu, M. In situ synthesis of TiO₂@NH₂-MIL-125 composites for use in combined adsorption and photocatalytic degradation of formaldehyde. *Appl. Catal. B Environ.* **2019**, *259*, 118106. [[CrossRef](#)]
26. Li, Y.; Chen, X.; Wang, C.; Zhang, C.; He, H. Sodium Enhances Ir/TiO₂ activity for catalytic oxidation of formaldehyde at ambient temperature. *ACS Catal.* **2018**, *8*, 11377–11385. [[CrossRef](#)]
27. Li, X.; Li, H.; Huang, Y.; Cao, J.; Huang, T.; Li, R.; Zhang, Q.; Lee, S.-c.; Ho, W. Exploring the photocatalytic conversion mechanism of gaseous formaldehyde degradation on TiO_{2-x}-O_v surface. *J. Hazard. Mater.* **2022**, *424*, 127217. [[CrossRef](#)]
28. He, F.; Jeon, W.; Choi, W. Photocatalytic air purification mimicking the self-cleaning process of the atmosphere. *Nature Commun.* **2021**, *12*, 2528. [[CrossRef](#)]
29. Wang, X.; Hong, S.; Lian, H.; Zhan, X.; Cheng, M.; Huang, Z.; Manzo, M.; Cai, L.; Nadda, A.; Le, Q.V.; et al. Photocatalytic degradation of surface-coated tourmaline-titanium dioxide for self-cleaning of formaldehyde emitted from furniture. *J. Hazard. Mater.* **2021**, *420*, 126565. [[CrossRef](#)]
30. Deng, X.-Q.; Zhu, X.; Sun, Z.-G.; Li, X.-S.; Liu, J.-L.; Shi, C.; Zhu, A.-M. Exceptional activity for photocatalytic mineralization of formaldehyde over amorphous titania nanofilms. *Chem. Eng. J.* **2016**, *306*, 1001–1009. [[CrossRef](#)]
31. Kresse, G.; Furthmüller, J. Efficiency of ab-initio total energy calculations for metals and semiconductors using a plane-wave basis set. *Comp. Mater. Sci.* **1996**, *6*, 15–50. [[CrossRef](#)]
32. Kresse, G.; Furthmüller, J. Efficient iterative schemes for ab initio total-energy calculations using a plane-wave basis set. *Phys. Rev. B* **1996**, *54*, 11169–11186. [[CrossRef](#)]
33. Perdew, J.P.; Burke, K.; Ernzerhof, M. Generalized gradient approximation made simple. *Phys. Rev. Lett.* **1996**, *77*, 3865–3868. [[CrossRef](#)]
34. Kresse, G.; Joubert, D. From ultrasoft pseudopotentials to the projector augmented-wave method. *Phys. Rev. B* **1999**, *59*, 1758–1775. [[CrossRef](#)]
35. Blöchl, P.E. Projector augmented-wave method. *Phys. Rev. B* **1994**, *50*, 17953–17979. [[CrossRef](#)] [[PubMed](#)]
36. Choudhury, B.; Choudhury, A. Oxygen vacancy and dopant concentration dependent magnetic properties of Mn doped TiO₂ nanoparticle. *Curr. Appl. Phys.* **2013**, *13*, 1025–1031. [[CrossRef](#)]
37. Huang, H.; Hou, X.; Xiao, J.; Zhao, L.; Huang, Q.; Chen, H.; Li, Y. Effect of annealing atmosphere on the performance of TiO₂ nanorod arrays in photoelectrochemical water splitting. *Catal. Today* **2019**, *330*, 189–194. [[CrossRef](#)]
38. Dutta, S.; Chattopadhyay, S.; Jana, D.; Banerjee, A.; Manik, S.; Pradhan, S.K.; Sutradhar, M.; Sarkar, A. Annealing effect on nano-ZnO powder studied from positron lifetime and optical absorption spectroscopy. *J. Appl. Phys.* **2006**, *100*, 114328. [[CrossRef](#)]
39. He, Y.; Dulub, O.; Cheng, H.; Selloni, A.; Diebold, U. Evidence for the predominance of subsurface defects on reduced anatase TiO₂ (101). *Phys. Rev. Lett.* **2009**, *102*, 106105. [[CrossRef](#)]
40. Sun, W.; Li, Y.; Shi, W.; Zhao, X.; Fang, P. Formation of AgI/TiO₂ nanocomposite leads to excellent thermochromic reversibility and photostability. *J. Mater. Chem.* **2011**, *21*, 9263–9270. [[CrossRef](#)]
41. Liu, Y.; Chen, P.; Fan, Y.; Fan, Y.; Shi, X.; Cui, G.; Tang, B. Grey rutile TiO₂ with long-term photocatalytic activity synthesized via two-step calcination. *Nanomaterials* **2020**, *10*, 920. [[CrossRef](#)]
42. Huang, J.; Yang, K.; Zhang, Z.; Yang, L.; Hirano, S. Layered perovskite LiEuTiO₄ as a 0.8 V lithium intercalation electrode. *Chem. Commun.* **2017**, *53*, 7800–7803. [[CrossRef](#)] [[PubMed](#)]
43. Lee, J.W.; Moon, B.M.; Lee, K.M.; Kim, Y.H.; Park, H.G.; Lim, J.H.; Oh, B.Y.; Kim, B.Y.; Hwang, J.Y.; Ok, C.H.; et al. Homogeneous liquid crystal orientation on ion beam exposure TiO₂ surfaces depending on an anisotropic dipole field. *Liq. Cryst.* **2010**, *37*, 279–284. [[CrossRef](#)]
44. Shi, C.; Qi, H.; Sun, Z.; Qu, K.; Huang, Z.; Li, J.; Dong, M.; Guo, Z. Carbon dot-sensitized urchin-like Ti³⁺ self-doped TiO₂ photocatalysts with enhanced photoredox ability for highly efficient removal of Cr⁶⁺ and RhB. *J. Mater. Chem. C* **2020**, *8*, 2238–2247. [[CrossRef](#)]
45. Li, G.; Lian, Z.; Li, X.; Xu, Y.; Wang, W.; Zhang, D.; Tian, F.; Li, H. Ionothermal synthesis of black Ti³⁺-doped single-crystal TiO₂ as an active photocatalyst for pollutant degradation and H₂ generation. *J. Mater. Chem. A* **2015**, *3*, 3748–3756. [[CrossRef](#)]
46. Guillemot, F.; Porté, M.C.; Labrugère, C.; Baquey, C. Ti⁴⁺ to Ti³⁺ conversion of TiO₂ uppermost layer by low-temperature vacuum annealing: Interest for titanium biomedical applications. *J. Colloid Interf. Sci.* **2002**, *255*, 75–78. [[CrossRef](#)] [[PubMed](#)]

47. Hu, Z.; Yu, J.C.; Ming, T.; Wang, J. A wide-spectrum-responsive TiO₂ photoanode for photoelectrochemical cells. *Appl. Catal. B Environ.* **2015**, *168–169*, 483–489. [[CrossRef](#)]
48. Qian, A.; Hyeon, S.E.; Seo, J.Y.; Chung, C.-H. Capacitance changes associated with cation-transport in free-standing flexible Ti₃C₂T_x (T=O, F, OH) MXene film electrodes. *Electrochim. Acta* **2018**, *266*, 86–93. [[CrossRef](#)]
49. Qiu, H.; Ma, X.; Sun, C.; Zhao, B.; Chen, F. Surface oxygen vacancies enriched Pt/TiO₂ synthesized with a defect migration strategy for superior photocatalytic activity. *Appl. Surf. Sci.* **2020**, *506*, 145021. [[CrossRef](#)]
50. Xu, K.; Yang, X.; Sun, D.; Yang, X.; Zhou, Y.; Li, W.; Yang, Q.; Yang, X.; Li, R.; Feng, J. Enhanced visible-light driven photocatalytic performances over LaFeO₃/NiO modified porous g-C₃N₄ nanosheets. *Nano* **2019**, *15*, 2050010. [[CrossRef](#)]
51. Gu, Y.H.; Fujimiya, Y.; Kunugita, N. Long-term exposure to gaseous formaldehyde promotes allergen-specific IgE-mediated immune responses in a murine model. *Hum. Exp. Toxicol.* **2008**, *27*, 37–43. [[CrossRef](#)]
52. Alminshid, A.H.; Abbas, M.N.; Alalwan, H.A.; Sultan, A.J.; Kadhom, M.A. Aldol condensation reaction of acetone on MgO nanoparticles surface: An in-situ drift investigation. *Mol. Catal.* **2021**, *501*, 111333. [[CrossRef](#)]
53. Li, J.; Cui, W.; Chen, P.; Dong, X.A.; Chu, Y.; Sheng, J.; Zhang, Y.; Wang, Z.; Dong, F. Unraveling the mechanism of binary channel reactions in photocatalytic formaldehyde decomposition for promoted mineralization. *Appl. Catal. B Environ.* **2020**, *260*, 118130. [[CrossRef](#)]
54. Jodłowski, P.J.; Jędrzejczyk, R.J.; Chlebda, D.; Gierada, M.; Łojewska, J. In situ spectroscopic studies of methane catalytic combustion over Co, Ce, and Pd mixed oxides deposited on a steel surface. *J. Catal.* **2017**, *350*, 1–12. [[CrossRef](#)]
55. Song, S.; Lu, C.; Wu, X.; Jiang, S.; Sun, C.; Le, Z. Strong base g-C₃N₄ with perfect structure for photocatalytically eliminating formaldehyde under visible-light irradiation. *Appl. Catal. B Environ.* **2018**, *227*, 145–152. [[CrossRef](#)]
56. Lu, J.; Zhong, J.; Ren, Q.; Li, J.; Song, L.; Mo, S.; Zhang, M.; Chen, P.; Fu, M.; Ye, D. Construction of Cu-Ce interface for boosting toluene oxidation: Study of Cu-Ce interaction and intermediates identified by in situ DRIFTS. *Chin. Chem. Lett.* **2021**, *32*, 3435–3439. [[CrossRef](#)]
57. Xu, P.; Xu, T.; Yu, H.; Zheng, D.; Li, X. MOF (metal-organic framework) nanomaterial for 400 ppb-concentration detectable xylene gas sensors. In Proceedings of the 2017 IEEE 30th International Conference on Micro Electro Mechanical Systems (MEMS), Las Vegas, NV, USA, 22–26 January 2017; pp. 1075–1078.
58. Hu, Z.; Yang, C.; Lv, K.; Li, X.; Li, Q.; Fan, J. Single atomic Au induced dramatic promotion of the photocatalytic activity of TiO₂ hollow microspheres. *Chem. Commun.* **2020**, *56*, 1745–1748. [[CrossRef](#)] [[PubMed](#)]
59. Jiang, B.; Zheng, J.; Qiu, S.; Wu, M.; Zhang, Q.; Yan, Z.; Xue, Q. Review on electrical discharge plasma technology for wastewater remediation. *Chem. Eng. J.* **2014**, *236*, 348–368. [[CrossRef](#)]
60. Oinuma, G.; Nayak, G.; Du, Y.; Bruggeman, P.J. Controlled plasma—Droplet interactions: A quantitative study of OH transfer in plasma–liquid interaction. *Plasma Sources Sci. Technol.* **2020**, *29*, 095002. [[CrossRef](#)]